



Nanoscale

**The Impact of Spatially Heterogeneous Chemical Doping on
the Electronic Properties of CdSe Quantum Dots: Insights
from ab initio Computation**

Journal:	<i>Nanoscale</i>
Manuscript ID	NR-ART-08-2023-004342.R1
Article Type:	Paper
Date Submitted by the Author:	22-Sep-2023
Complete List of Authors:	Deswal, Priyanka ; IIT Delhi, Dept. Physics Samanta, Kushal; IIT Delhi, Dept. Materials Science and Engg. Ghosh, Dibyajyoti; IIT Delhi,

SCHOLARONE™
Manuscripts

The Impact of Spatially Heterogeneous Chemical Doping on the Electronic Properties of CdSe Quantum Dots: Insights from *ab initio* Computation

Priyanka Deswal,^a Kushal Samanta,^b Dibyajyoti Ghosh^{bc*}

^a Department of Physics, Indian Institute of Technology, Delhi, Hauz Khas, New Delhi 110016, India

^b Department of Materials Science and Engineering, Indian Institute of Technology, Delhi, Hauz Khas, New Delhi 110016, India

^c Department of Chemistry, Indian Institute of Technology, Delhi, Hauz Khas, New Delhi 110016, India

* Corresponding authors; E-mails: dibyajyoti@iitd.ac.in

Abstract

The introduction of copper (Cu) impurity in semiconductor CdSe quantum dots (QDs) gives rise to unique photoluminescence (PL) bands exhibiting distinctive characteristics, like broad line width, significant Stokes shift, and complex temporal decay. The atomistic origins of these spectral features are yet to be understood comprehensively. We employ multiple computational techniques to systematically study the impact of spatial heterogeneity of Cu atoms on the stability and photophysical properties, including the emission linewidth of doped QDs at ambient conditions. The Cu substitution introduces a spin-polarized intragap state, the energetic

position of which is strongly dependent on the dopant location and causes spectral broadening in QD ensembles. Furthermore, the dopant dynamics at ambient conditions are significantly influenced by the specific arrangement of Cu within QDs. The dynamic electronic structures of surface-doped CdSe illustrate more pronounced perturbations and vary the mid-gap state position more drastically than those of the core-doped QD. The vibronic coupling broadens the photoluminescence peaks associated with the conduction band-to-defect level transition for individual QDs. These insights into the dynamic structure – photophysical properties relationship suggest viable approaches, such as tuning the operational temperature and selective co-doping, to enhance the functional performances of doped CdSe QDs strategically.

Introduction

Inorganic colloidal quantum dots (QDs) are promising candidates for optoelectronics due to their highly tuneable unique luminescence characteristics.¹⁻³ These nanoscale semiconductor particles emitting light in visible and near-infrared regions are highly valuable for bioimaging, solar energy conversion, and light-emitting diodes.³⁻⁸ Due to the dominant quantum confinement effect, the optical characteristics heavily rely on the size, shape, and composition of these QDs.⁹⁻¹² Among several candidates, cadmium selenide (CdSe) QDs are investigated extensively for their direct optical bandgap, visible light emission, adjustable emitting light color, and narrow luminescence linewidth.¹³⁻¹⁶ These properties make the CdSe QDs suitable for various applications such as LEDs, solar cells, laser, and biological sensors.^{15,17,18} Various organic and inorganic ligands are used to stabilize these QDs by surface passivation.¹⁹ The ligand passivation mitigates surface defect states and significantly influences the photophysical properties like band gap, spectral diffusion, and fluorescence lifetime.^{20,21} These effects further play a crucial role in determining the emission quality and efficiency of QDs.^{22,23}

The extrinsic impurity incorporation via controlled ion exchange is a widely explored approach to tune the physicochemical properties and optoelectronics of semiconductor QDs.^{24–26} The doped QDs with transition metal ions such as Cu, Ag, Mn, or Co can enhance optical properties, improve stability, increase carrier confinement, and tailor electronic properties.^{27–30} The Cu-doping into II-VI QDs is extensively investigated as it introduces intragap states that actively participate in optical transitions.^{31,32} The radiative recombination of delocalized conduction band electron and localized hole at the Cu site gives rise to distinct photoluminescence (PL) band and long excited state lifetimes.^{33–36} These chemically modified QDs also offer functional advantages such as reduced reabsorption, efficient light conversion, and tunability, proposing their unique applications.^{37–39} The creation of localized defect states indicates well-defined and indistinguishable photon emission.³⁷ These characteristics are desirable for single photon emitters, enabling efficient coupling of emitted photons to optical fibers.^{40,41} The localized midgap states in QDs further facilitate efficient light absorption and generate free charge carriers in photovoltaic devices, enhancing their performance efficiency.⁴²

Despite significant progress in understanding the fundamental properties of Cu-doped semiconductors and integrating them in various optoelectronic devices, several photophysical characteristics still need to be optimized to boost their functionalities.³⁹ A primary concern is the significant Stokes shift of ~ 200 meV observed in Cu-doped CdSe QDs.^{39,43} The Cu inclusion also results in considerable bandwidth (full width at half-maximum (fwhm)) broadening and reducing the PL spectra's spectral resolution.^{8,39} The fwhm of the dopant-induced PL peak is of the order of 300-500 meV, which is much higher than the band edge-related excitonic PL peaks.⁴⁴ Such a phenomenon hinders the accurate measurement of spectral properties of doped QDs and restricts their potential applications in sensing and imaging.⁴⁵ Additionally, the broad PL band shape of Cu-CdSe QDs makes it less suitable for high-resolution spectroscopy.⁴⁶ The decay characteristics of Cu-induced PL are multiexponential and exhibit a long lifetime due to the localized nature of acceptor levels.^{8,47} The

multiexponential feature of PL decay indicates a significant lifetime that can originate from factors like different radiative transition probabilities, the inclusion of extrinsic non-radiative processes, and enhanced electron-phonon interactions.³⁶

Many detailed studies have pointed out that the special distribution of Cu in the QDs introduces significant heterogeneity in terms of their emission characteristics.^{8,27,47} The much narrower PL linewidth of a single QD than that of the ensemble confirms considerable dot-to-dot variation in photoactivity. The relatively broad defect-associated PL linewidth at low-temperature also indicates the intrinsic positional inequivalence of Cu in the lattice most likely contributes to the electron-hole recombination processes.⁴⁴ In that regard, the fluorescence line narrowing technique has shown that the nonuniformity of Cu dopants in terms of the chemical environment considerably broadens the associated emission line.^{44,47} The modification of the local coordination environment, lattice distortion, and changes in the site symmetry of dopant atoms in semiconductor hosts are recognized as crucial factors.^{37,47} Apart from heterogeneous chemical bonding, the large fwhm (~ 325 meV) of defect PL peak even for single Cu-doped QD at room temperature, is attributed to the strong electron-phonon interactions.⁴⁸ These vibronic couplings lead to substantial atomic rearrangement around the dopant in an excited state, causing broadening of the band shape of the PL line.⁴⁹ The large electron-phonon coupling for the localized hole state contributes to the emission broadening in these doped QDs.⁵⁰ Thus, the complex interactions between electronic and vibrational subsystems significantly modify the emission profile of CdSe QDs.^{50–52} However, a detailed atomistic understanding of dynamic structure–excited state properties is largely missing for these nanomaterials. An in-depth study on the influence of structural vibrations on the functional properties of CdSe QDs will provide doping and co-doping strategies for improving their performances.^{27,29,30,39,45,46,53,54}

In this work, we explore the effects of positional heterogeneity of Cu dopants on the optoelectronic properties of CdSe QDs. The detailed computational study shows that Cu-doping incorporates a spin-polarized mid-gap state. The energetic position of this state strongly

depends on the dopant location inside the QD. The Cu at the core region results in an impurity level close to the valence band maximum (VBM), whereas surface doping causes a relatively deeper defect state. The local lattice contraction and antibonding overlap between 3d (Cu) and 4p (Se) orbitals shift the defect state deep into the band gap for surf-QD. The *ab initio* molecular dynamics (AIMD) simulations at ambient conditions further reveal significant dopant position-dependent structural fluctuations in these CdSe QDs. The time-dependent electronic properties depict that the Cu on the surface is more sensitive to thermal fluctuations resulting in widely distributed impurity levels inside the electronic gap. Influence spectra analysis further shows the stronger vibronic coupling for the impurity state in surface-doped QD. The diffused intra-gap state can significantly compromise the color purity and single photon emission quality of defect-state-induced light in these QDs. These insights reveal atomistic details of the dynamic structure–electronic properties relationship that governs the optoelectronics of modified QDs. Our study also provides a road map for strategic modifications to improve the functional properties of these QDs for next-generation devices.

Results and Discussion:

The magic-sized $\text{Cd}_{33}\text{Se}_{33}$ QD is considered the host for exploring the effects of Cu-doping in these nanomaterials (Figure 1a-d, Section S1). Several experimental studies have successfully synthesized and characterized these magic-sized QDs.^{31,53,55–58} After unconstrained geometry optimization of $\text{Cd}_{33}\text{Se}_{33}$, all Cd/Se atoms become at least a 3-coordinated state and consequently exhibit a defect-free electronic gap (Figure S1).⁵⁹ This predominantly spherical QD has a wide bandgap of 1.68 eV. Compared to the experimental one, the underestimation of the computed bandgap value originates from the semi-local exchange-correlation functional employed in all DFT calculations.^{60,61} The band edge charge densities are mostly delocalized over the whole QD (Figure 1e (right panel)). Notably, the valence band maximum (VBM) exhibits relatively less delocalization compared to the conduction band minimum (CBM).

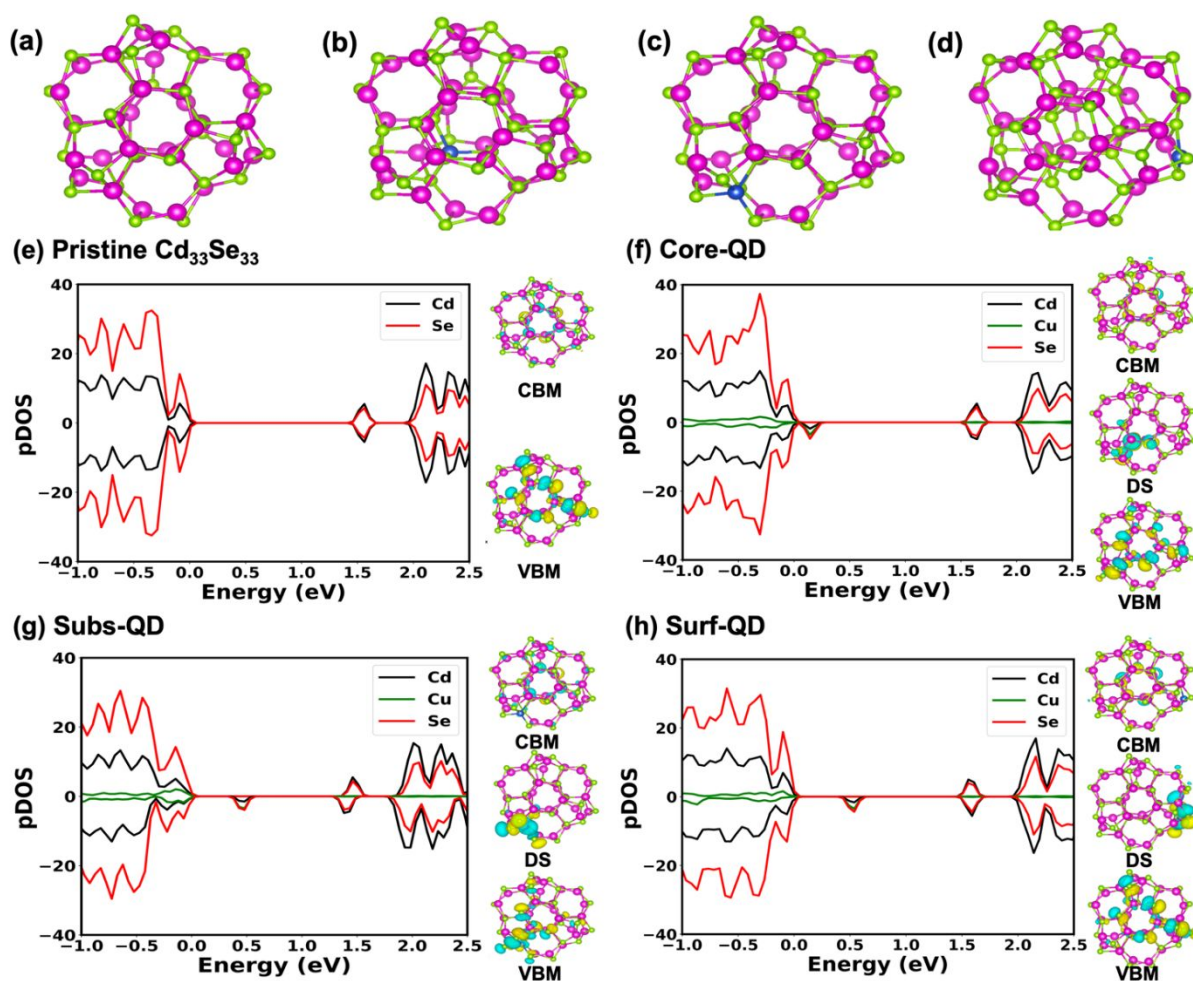


Figure 1. Optimized structures of (a) pristine $\text{Cd}_{33}\text{Se}_{33}$ and doped QD having Cu in (b) core (core-QD), (c) subsurface (sub-QD), and (d) surface (surf-QD). Partial density of states (pDOS) and charge density (right panel) of (e) pristine $\text{Cd}_{33}\text{Se}_{33}$, (f) core-QD, (g) sub-QD, and (h) surf-QD. Geometric optimization in these QDs mitigates the effect of dangling bonds and enhances structural stability. The molecular Kohn-Sham states are broadened by introducing a smearing factor of $\sigma=0.05$ for all convoluted pDOS plots. Colors: copper (blue), cadmium (purple), and selenium (green). We scale the edge of the thermally broadened HOMO state to 0 eV and consider it as the Fermi level.

In the computational model of doped-QDs, we replace a single Cd atom within the optimized $\text{Cd}_{33}\text{Se}_{33}$ with a Cu atom (Figure 1b-d). To explore the impact of Cu^{2+} -dopant's position on photophysical properties and structural dynamics, we examine three distinct sites within

$\text{Cd}_{32}\text{Se}_{33}\text{Cu}$, where the substituted Cu atom resides in the core (core-QD), subsurface (sub-QD), and surface (surf-QD) region (Figure 1b-d). Due to the low-symmetry structure of the surface reconstructed $\text{Cd}_{33}\text{Se}_{33}$, we consider multiple spatially distinct sites for Cu doping, as detailed in Section S2 of SI. The electronic structures of these doped QDs are discussed further (Figure 1f-h).

Static Structural Properties: As tabulated in Table 1 for all three configurations, the negative formation enthalpies indicate that substitutional Cu doping in CdSe QD is an energetically favorable process. The more covalent nature of newly formed Cu-Se bonds than pristine Cd-Se makes the overall substitution process thermodynamically exothermic. The relatively mild synthesis processes further support this energetically favourable Cu-doping of CdSe QDs.⁶⁰ The total potential energies and formation enthalpies (Table 1) further reveal that surface-doping is the most energetically favourable among the three sites considered here (Figure S3a). Thus, Cu might migrate from the core to the surface of QDs through diffusion. Such a phenomenon can lead to the self-purification of Cu-doped QDs, where the surface acts as a sink for the dopant atom.⁶² Several experimental studies have reported this diffusion-induced expulsion of dopant atoms from semiconductor QDs.^{60,62,63} The dopant dynamics and diffusion in these QDs are discussed later in the context of lattice fluctuations. Note that the formation enthalpy values, and corresponding spontaneity of Cu-doping are not solely determined by the intrinsic properties of the material and strongly depend on the size of QDs and the chemical environment of synthesis processes.^{58,64,66}

We closely investigate the local structural distortions near the Cu site (Figure 2a). Regarding the coordination environment, core and subsurface Cu atoms remain in tetrahedral (T_d) geometry, whereas the dopant on the surface forms a distorted trigonal planar geometry (Figure 2b, S1). Primarily due to the smaller ionic size of Cu (radii 73 pm) than that of Cd (radii 97 pm), Cu-Se exhibits shorter bond lengths, inducing local compressive strain around the dopant atom (Figure 2a, S2). Compared to equivalent Cd-Se bonds in $\text{Cd}_{33}\text{Se}_{33}$, the Cu-Se

contract 8.4%, 8.6%, and 9.9% for the core-QD, sub-QD, and surf-QD, respectively (Figure S3b). Experimental reports based on extended X-ray absorption fine structure (EXAFS) also support the observation of local lattice contraction due to Cu incorporation in similar II-VI semiconductors.^{54,65,66} The lower coordination number and higher degrees of freedom allow the surface Cu-Se bonds to contract more, incorporating a more significant distortion than that in core- and sub-QD (Figure 2a and S3b). Such controlled inclusion of surface strain significantly tunes the physicochemical properties, including catalytic performances of nanocrystals.^{67,68} Overall, the total energy calculations illustrate that shorter surface Cu-Se bond formation relaxes the local dopant environment and predominantly stabilizes the surf-QD. These insights emphasize the heterogeneity in Cu-Se bonding arising due to different spatial positions of the dopant atom in CdSe QD.

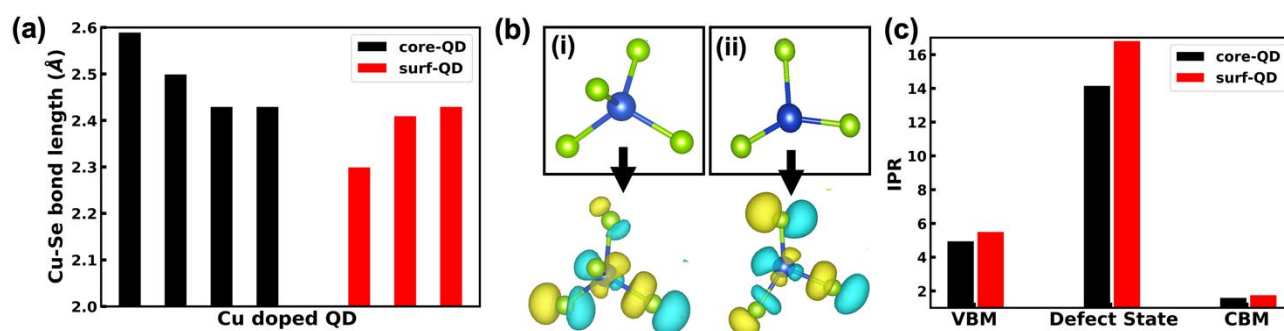


Figure 2: (a) Bar graph of individual Cu-Se bond lengths (local structural distortions) of doped CdSe QD with Cu in the core and on the surface. (b) The local coordination environment (above panel) and antiphase overlapping (bottom panel) of (i) core Cu with tetrahedral (T_d) and (ii) surface Cu with distorted trigonal planar geometries in $Cd_{32}Se_{33}Cu$. Isosurface value is $0.005 \text{ e}\text{\AA}^{-3}$ (c) Inverse participation ratio (IPR) of the valence band maximum (VBM), defect-state, and conduction band minimum (CBM) for core- and surf-QDs.

To explore the influence of ligand passivation on Cu-doped CdSe QDs, we consider three commonly used molecules: methyl amine (NH_2Me , $Me = CH_3$), methyl phosphine (PH_2Me), and trimethyl phosphine oxide ($OPMe_3$) (Figure S6).^{69,70} These small molecules represent the

experimentally used long-alkyl-chain passivating ligands.^{19,22} The geometry optimization of these ligand-passivated QDs exhibits minimal modifications on the surface structure compared to their bare counterpart (SI, Section S4, Table S1). The high stability of these magic-sized bare QDs primarily prevents ligand-induced surface reconstructions.⁷¹

Static Electronic Properties: The electronic structures of doped QDs exhibit that the Cu incorporation introduces an in-gap p-type defect state in the minority spin channel (Figure 1f-h, S5). Note that our calculations consistently find a +2-oxidation state and corresponding 3d⁹ configuration of the Cu, regardless of its location in these QDs (Section S3 in SI). This is in agreement with experimental studies, where the unpaired 3d electron in the Cu dopant introduces net magnetic moment in these doped QDs.^{72,73} Several experimental studies have also reported the presence of a hole-like state in Cu-doped CdSe, which acts as a pinned acceptor level.^{27,29} Furthermore, the energy state position of this 100% spin-polarized acceptor level is specific to the location of Cu (Table 1). The plotted partial density of states (pDOS) in Figure 1f-h exhibits the impurity level for core-, sub-, and surf-QD at 0.23 eV, 0.58 eV, and 0.63 eV above the VBM, respectively. Thus, the defect state shifts deeper in the bandgap as the Cu atom moves from the core to the surface of CdSe QD. The strong influence of the location of Cu-site on the intragap defect-state energetics indicates the considerable QD-to-QD variation in emission and carrier lifetime, as already reported by several experimental studies.^{44,74,75}

Table 1. The structural and electronic properties of core, sub, and surf-QDs.

	Average bond length Cu-Se (Å)	Formation enthalpy (eV)	Defect state position (Above VBM) (eV)	Elemental Contribution in defect state (%)			Bader charge on Cu (e ⁻)
				Se	Cu	Cd	
Core-QD	2.49	-1.27	0.23	43	41	16	+0.45
Sub-QD	2.52	-1.31	0.58	46	37	17	+0.49
Surf-QD	2.38	-1.48	0.62	45	38	17	+0.46

Table 1 includes the Bader charges of host and dopant atoms. The lesser positive charge on Cu (+0.68 e^-) compared to Cd highlights the more covalent and less polar nature of Cu-Se than that of Cd-Se bonds. This change in local bonding nature is further illustrated by the charge density differences shown in Figure S11. The higher charge depletion around Cd (as indicated by blue-colored isosurface in Figure S11) than that around dopant Cu in doped-QDs depicts the relatively higher charge transfer between Cd and Se in $\text{Cd}_{33}\text{Se}_{33}$. Note that very similar Bader charges for Cu atoms designate that the overall charge state of the dopant remains consistent regardless of its spatial positions in this QD. The pDOS plots, charge densities (Figure 1f-h and right panel), and Table 1 show that mostly Se (43-46%) and Cu (37-41%) with a minor contribution from Cd (16-17%) form the mid-gap state. The VBM and CBM of these doped QDs remain largely delocalized over Cd and Se atoms with minor participation of Cu orbitals. Thus, similar electronic characteristics in band edges and mid-gap state cannot explain the variation in the in-gap state positions of Cu-doped QDs.

We further focus on the orbital interactions in the mid-gap state and their dependence on the local structure of Cu. Figure 2b represents the antiphase (antibonding) overlaps between 3d of Cu and 4p of neighbouring Se's that predominantly contribute to the formation of intragap state in Cu-doped CdSe. This results in a significant p-d hybridization between Cu and Se atoms.⁷⁶ Here, we mainly consider pristine, surf-, and core-QDs for further investigations revealing detailed structure–electronic property relationships. Broadly, two main geometrical features alter with the Cu position: (a) the coordination environment of the dopant and (b) the bond lengths between Cu-Se. Considering local geometries, the core- and sub-QD have Cu in tetrahedral coordination, whereas surf-QD exhibits a distorted trigonal coordination for dopant. However, we later discover in our study of dynamic structures that this apparent coordination difference does not significantly impact the defect level position at ambient conditions. On the contrary, the Cu-Se bond distances play a crucial role in determining the position of the intragap state in these doped QDs. The shorter surface Cu-Se bonds enforce a more pronounced

antibonding overlap between Cu 3d and Se 4p, as shown in Figure 2b. This orbital interaction shifts the defect state deeper into the bandgap for sub- and surf-QDs (Figure 1g, h).⁸ The partial local relaxation of Cu-site in core-QDs causes less contraction in Cu-Se bonds (Figure 2a), allowing the in-gap state to remain relatively closer to the VBM state (Figure 1f).

To quantify the charge localization in the defect state, we calculate the inverse participation ratios (IPR) and include those in Figure 2c. From the adopted definition, the higher charge delocalization in an electronic state corresponds to a lower value of IPR. In Figure 2c, the band edge states have lower IPR values due to their delocalized charge densities. These charge delocalization and associated IPR values are not significantly impacted by the position of Cu within the QD. However, the in-gap state exhibits a higher IPR value for surf-QD, indicating a more robust charge localization than the core-QD. The higher degree of charge localization in the anti-bonding intragap state further explains its shift away from the valence band edge in the surf-QD. As reported, CdSe QDs with two-coordinated Se atoms on the surface also show charge localization and in-gap defect state formation.³⁷

To further verify the subtle impact of dopant-Se bond length on the defect-state position, we replace surface Cu with Ag, which has a larger ionic radius than Cu. The relaxed geometry shows that the Ag-Se bonds are longer than Cu-Se bonds by ~ 0.2 Å on average shown in Figure S11e. As shown in Figure S11f, the increased dopant-Se bond length subsequently drives the defect state closer to the VBM state (0.38 eV above VBM). Thus, the position of the in-gap state can be tuned by precisely changing the coordination environment of the dopant on the surface of the CdSe QDs. These analyses also prove that the dopant-Se bond distances are the dominant factor that controls the defect properties of QDs.

To understand the effects of ligands on the electronic properties, we plot the pDOS of NH₂Me, PH₂Me, and OPMe₃ passivated Cd₃₂Se₃₃Cu in Figures S7-S9. Irrespective of ligand type, these simulations find that the passivated QDs exhibit a deeper mid-gap state for surface-doped Cu than the core-doped one. The overall charge density distributions in the VBM, CBM, and spin-

polarized mid-gap defect state remain primarily unchanged for bare and passivated QDs (Figure S8-S10 (right panel)). Thus, the ligand passivation does not substantially impact the overall electronic properties of doped CdSe (see Section S4 in the SI for details).

Several studies have shown that a solvent environment can significantly modify the electronic and optical properties of QDs.^{77,78} However, our calculations demonstrate that the overall electronic states of Cu-QDs remain mostly unaltered while considering water as an implicit solvent (Figure S12). Thus, we continue molecular dynamics simulations considering gas-phase as the environment for these QDs.

Dynamic Structural Properties: The structural dynamics at ambient conditions are crucial in determining functional properties, including emission and optoelectronics in nanomaterials.^{44,79–81} Thus, we perform AIMD simulations to explore the impacts of Cu-doping in Cd₃₃Se₃₃ QD at 300 K. The long enough equilibrated trajectories of >15 ps have been simulated to ensure reliable results from these in-silico studies. The plotted potential energy and temperature over simulation time show the adequate equilibration of the pristine and doped CdSe QDs at 300 K (Figure S13a-d). The visual inspection of the trajectories demonstrates the structural integrity of these QDs for the entire simulation time (watch the movies in Supplementary Information). The plotted pair distribution functions $g(r)$ for Cd-Se and Cu-Se in Figure S14a also show the narrow distribution of bond distances within 2-3 Å, confirming the stable geometric structures of QDs. We evaluate the root-mean-square fluctuations (RMSF) to quantify the extent of thermal fluctuations of individual or groups of atoms for these nanomaterials. Separating the QD into surface and core regions, the evaluated RMSFs reveal more thermal fluctuations for the surface atoms than the core ones (Figure S14b and Section S6). This general trend does not depend on the presence and spatial position of the Cu dopant in the CdSe QDs. As expected, the lower coordination results in a more dynamic surface in these 0-dimensional systems. One can find more elaborate discussions on the dynamics of pristine Cd₃₃Se₃₃ elsewhere.⁷⁰

We now focus on the impact of heterogeneity of dopant position on the energetics and structural dynamics in $\text{Cd}_{32}\text{Se}_{33}\text{Cu}$. Figure S13b and d illustrates that surf-QD has higher stability than the core-QD over simulated trajectories at ambient temperature. The surf-QD is more stable by 0.07 eV than core-QD as calculated from time-averaged potential energies. Thus, the dopant Cu atom has considerable site preference in these doped CdSe QDs at 300 K. The RMSF of all atoms, as shown in Figure S14b, enhanced by 8% and 1% for core- and surf-QD, respectively, compared to the pristine one (Section S6 for more details). Thus, the single Cu inclusion in the core does impact the overall dynamic nature of these QDs. Nonetheless, the computed trajectory ensures core-QD stability at 300 K as the Cu atom remains in the core site throughout the simulation. The detailed investigations further reveal that the dynamics of the Cu atom significantly depend on its spatial location. The RMSF of Cu in the core is 7% higher than the Cu on the surface, as shown in Figure 3a. The substitution of smaller-sized Cu^{2+} (0.73 Å) in place of larger Cd^{2+} (0.95 Å) provides an oversized tetrahedral void for the dopant to fluctuate in the core, resulting in higher RMSF for CuSe_4 tetrahedron (Figure 3a). On the contrary, the surface Cu remains in a trigonal planar geometry and has less space to fluctuate. The shorter bond length of Cu-Se on the surface also restricts the dopant dynamics (Figure 3c). Thus, we identify substantial heterogeneity in structural dynamics for doped-QDs with differently distributed dopants.

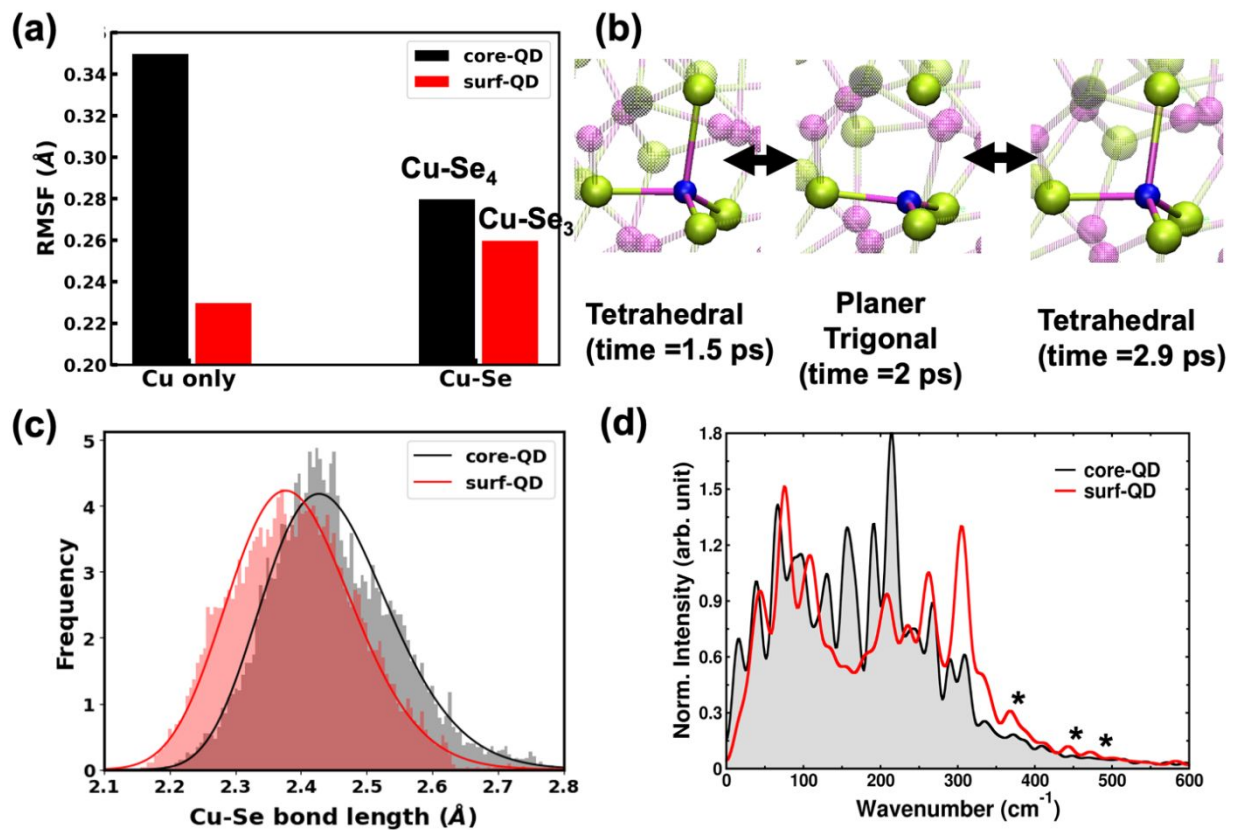


Figure 3: (a) Bar graph showing RMSF of only Cu atoms, doped in core and surface, and Cu and neighboring Se atoms for core-QD (CuSe₄ tetrahedron cluster) and surf-QD (CuSe₃ planar trigonal cluster). (b) The local coordination geometry of CuSe₄ over time shows the transformation of the core Cu atom from tetrahedral to planar trigonal (short-lived for 1.5ps) to tetragonal structure. (c) The histograms for Cu-Se bond distances in core-QD (only shortest 3 bonds) and surf-QDs. (d) Impact of Cu doping position in the partial vibrational density of states (vDOS) for core-QD and surf-QDs. The partial vDOSs include the contribution of the dopant atom only.

The simulated MD trajectory illustrates that the core Cu atom primarily occupies the tetrahedral site and forms four Cu-Se bonds over the simulation time. However, occasionally Cu also transforms its coordination geometry from tetrahedral to planar trigonal form and moves to one of the sides of the tetrahedron (Figure 3b). The planar trigonal coordination of Cu in the core is short-lived (~1.5 ps), and it returns to the tetragonal site relatively quickly (~0.9 ps). The

switching between two coordination geometries gives rise to the fluxional characteristics of small-sized Cu in the host QD. These structural dynamics also hint that Cu atoms may diffuse through the side of the CuSe_4 tetrahedron and can migrate to the surface of QDs at a high enough temperature to perform a self-purification process.^{60,62,63} Our attempt to visualize the core-to-surface Cu diffusion by simulating a longer trajectory of 18 ps of core-QD was unsuccessful. Therefore, we perform the climbing image nudged elastic band (CI-NEB)-based simulations that provide the energy barrier for ion migration in the solids.⁸² The diffusion barrier for Cu to migrate from core to surface is 0.69 eV, as shown in Figure S14c,d. The relatively large energy barrier indicates that the Cu diffusion requires high temperature in these QDs, well in agreement with the experimental findings.^{60,62,63} Further details of the NEB simulations and ion migration pathway are included in Section S5 and Figure S14c,d, SI.

The surface Cu does not change its overall coordination under ambient conditions and remains in strained trigonal planar geometry. In Figure 3c, we find that the surface Cu-Se bonds are shorter than that in the core at 300 K. Here, we exclude the largely fluctuating Cu-Se bond distance of core-QD. The median values of Cu-Se bond distances are 2.38 and 2.35 Å for the core and surface, respectively. As the Cu-Se bond distances subtly influence the intragap defect state position, these geometric variations impact the electronic and emission properties of doped QDs (discussed later). Overall, the core dopant distorts the local tetrahedral geometry and varies the Cu-Se bond distances more significantly than the Cu on the surface.

We further calculate the vibrational density of states (vDOS) for Cu-doped $\text{Cd}_{33}\text{Se}_{33}$ by performing a Fourier transformation of the velocity autocorrelation function of atoms (Figure 3d).⁸³ The combined spectroscopic techniques such as infrared and Raman spectroscopy provide similar information on the dynamics of the material. These vibrational features in nanometre-sized QDs are distinctly broader than the bulk CdSe.⁸⁴ The evaluated total vDOS with decomposed elemental contributions are shown in Figures S14a,b. All vibrational peaks mostly appear within 350 cm^{-1} for these QDs. The absence of high-energy vibrational peaks

qualitatively matches the available experimental data for CdSe QDs.^{85–87} There are a few common vibrational features irrespective of dopant position in the CdSe QD, (1) heavier Cd atoms mainly contribute to low-energy peaks at $<100\text{ cm}^{-1}$. These vibrational peaks are assigned as transverse acoustic (TA) phonon modes. (2) Higher energy peaks at $150\text{--}250\text{ cm}^{-1}$ have more contributions from vibrational modes, including Se atoms. These vibrational peaks are longitudinal acoustic (LA) and various optical modes. Previous reports assign the peaks of this range as transverse optical (TO), surface optical (SO), and longitudinal optical (LO) modes.^{88–90} However, we do not attempt to identify the exact origin of these modes due to the presence of broadened and overlapping peaks. (3) The dopant Cu dominates the highest vibrational energy range at $>250\text{ cm}^{-1}$.^{77,78} Focusing on the impact of dopant position on vibrational features, we closely investigate the corresponding vDOS, as shown in Figure 3d. The $250\text{--}500\text{ cm}^{-1}$ energy range is sensitive to the Cu dopant position. The surf-QD exhibits more pronounced narrow peaks at 262 cm^{-1} and 305 cm^{-1} than the core-QD. The Cu on the surface also introduces more vibrational peaks at $350\text{--}500\text{ cm}^{-1}$ marked with “*” in Figure 3d, indicating enhanced dopant dynamics. The lower coordination and irregular electrostatics on the surface introduce additional vibrational modes for Cu atoms in surf-QD. The vibrational distortion in the shorter and tightly bound surface Cu-Se bonds results in high energy peaks (Figure 3d). Therefore, the positional heterogeneity in doped-CdSe QDs directly influences the vibrational features.

Dynamic Electronic Properties: We next explore the influences of structural dynamics on the electronic properties of CdSe QDs. The vibrational modes give rise to enhanced electron-phonon interactions and significantly impact the energy states, band edge positions, and instantaneous band gaps of semiconductor QDs.^{16,44,55,91}

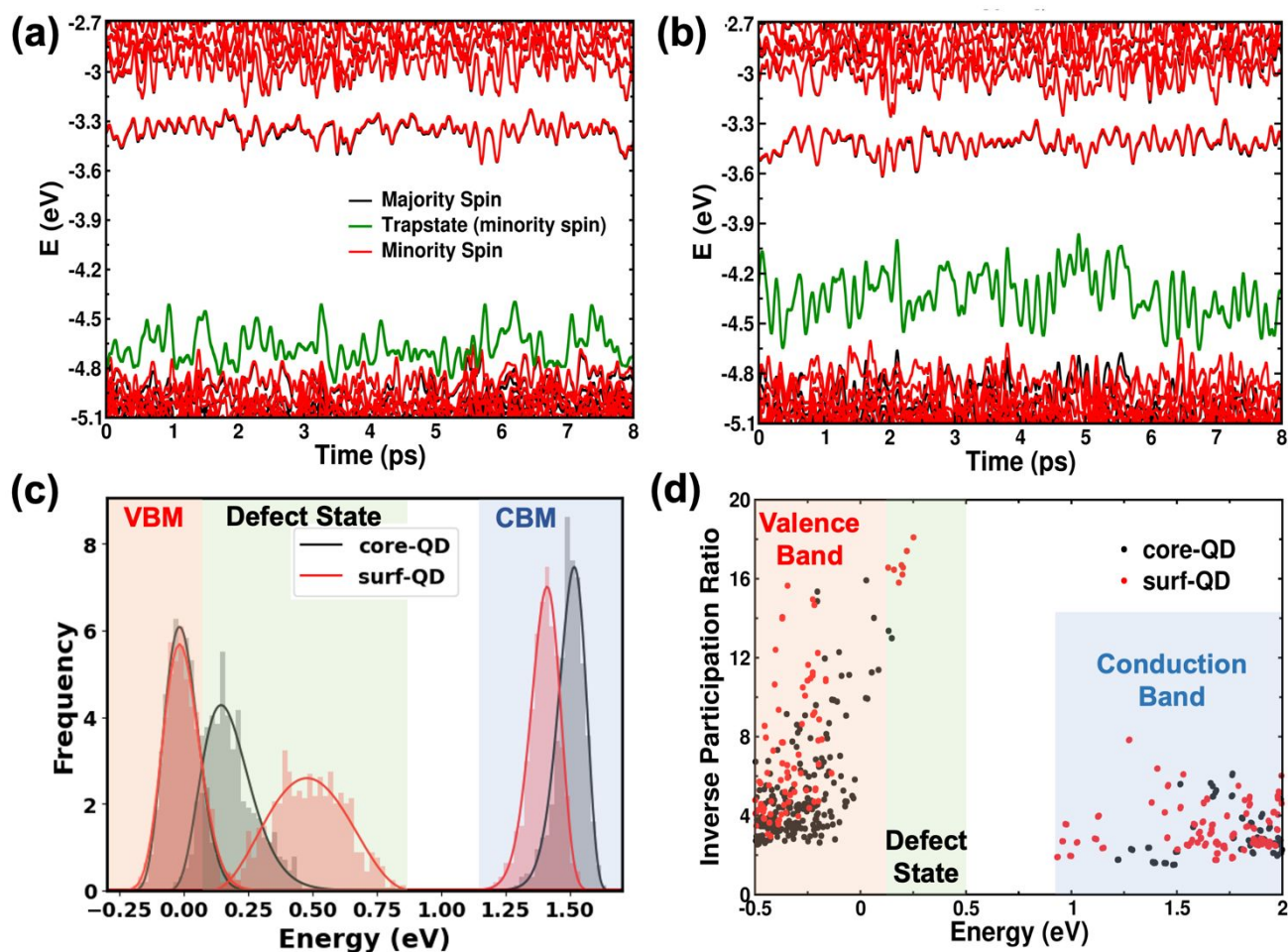


Figure 4. Electronic structure of QDs along the MD trajectories for (a) core-QD and (b) surf-QD, (c) Histogram of fluctuations in the energetic positions of band-edge states and defect state in minority spin channel for QDs. To align the energy states, we scale all band-edge energies of a particular system to their average VBM state energy, which then shifts to $E = 0$ eV. The band gap and band-edge energy distributions have been fitted with the β -distribution function plotted in the solid line with different colors, (d) IPR of electronic states from random instantaneous geometries along the MD trajectories of core- and surf-QD. Details are included in the SI, Section S5.

The band gap distribution of pristine $\text{Cd}_{33}\text{Se}_{33}$ shows the broadened peak, revealing its considerable variation over time (Section S7, Figure S16a). Likewise, for Cu-doped CdSe QDs, the VBM-defect state and defect state-CBM exhibit a wide distribution of energy gaps in the minority spin channel (Figure 4a,b and S15b,c). The varying energy gaps indicate the

significant impact of lattice vibrations on the absorption and emission properties of these QDs. The CBM state has the narrowest distribution among other band edge energy levels (Figure 4c, S16b). Relatively, the distribution of the VBM state is broader than that of the CBM (Figure 4c, S16a). The standard deviations for the VBM and CBM are in the range of 0.064-0.070 and 0.056-0.058 eV, respectively. The IPR of these band edge states provides the extent of charge localization at random instants of time along AIMD trajectories, as shown in Figure 4d. Considering these instantaneous structures, we find that the VBM state is much more localized than the CBM state, irrespective of dopant position in CdSe QDs. The charge density plots for these band edge states also show the localized and delocalized nature of the VBM and CBM states, respectively (Figure S16d-f). Thus, the extent of charge delocalization directly dictates the energetic distribution of these band edge states. The highly delocalized CBM state does not oscillate its position much, as the structural vibrational modes have a limited impact on its overall electronic characters. On the contrary, the VBM has more localized charge densities, dominantly on the surface-Se atoms. The fluctuations of these Se atoms give rise to more variation in the VBM state position, as shown in Figure 4c and S16a. So, the vibronic coupling strengths in these nanomaterials can vary for different band edge states. We further find that irrespective of dopant location, the spin-polarized mid-gap state position fluctuates much more than the band edge states as shown in Figure 4c. The fluorescence line narrowing-based experiment by Brovelli et al. shows a much narrower PL line width for band edge emission than the defect-state induced one, excellently matching our computational findings.⁴⁴ The charge density distributions at random time steps show that the defect state mostly remains localized in the $\text{CuSe}_4/\text{CuSe}_3$ cluster of CdSe QDs (Figure S16d-f). The calculated IPR values also exhibit more robust charge localization at the mid-gap states than at the band edge states of these doped QDs (Figure 4d). Thus, we conclude that the more the charge localization, the wider the distribution of the corresponding energy state at ambient conditions. These insights

on structural dynamics - electronic property relationships are invaluable for strategically modifying the nanomaterials for improved optoelectronics.

While overlooking the defect state, the VBM-CBM energy gap distributions for pristine and doped CdSe QDs are plotted in Figure S17c,d. We evaluate this gap for both spin channels in doped QDs (Section S7). The distributions are very similar for pristine Cd₃₃Se₃₃ and surf-QD. Irrespective of spin channels, the core-QD has a marginally narrow distribution of the energy gaps. The mode values of these distributions also show that the core-QD has a marginally higher CBM-VBM gap than the other two QDs. Thus, the band edge states are influenced by the presence and location of Cu atoms in CdSe QDs to some extent. In Figure 4b,c the mid-gap state is positioned much deeper in the band gap for the surf-QD than in the core-QD. Upon time-averaging, we find that the largely fluctuating defect states are on average 0.18 and 0.48 eV away from the VBM edge for core and surf-QD, respectively. The shorter Cu-Se distances (Figure 3c) and antibonding overlap (Figure S16f) primarily cause the deeper mid-gap formation for surf-QD at ambient conditions. Furthermore, the surf-QD has a much wider energetic distribution of the mid-gap state than the core-QD (Figure 4c). The standard deviations for this state are 0.098 and 0.14 for core and surf-QD, respectively. Due to the largely fluctuating mid-gap state position, the VBM-defect state and defect state-CBM energy gaps are much broader for surf-QD than for core-QD (Figure S18, 5a). The sizeable fluctuations in the defect state of surf-QD are caused dominantly by two factors, (a) high-energy vibrational modes of Cu atoms and (b) strongly localized charge density of this state. The presence of multiple high-frequency vibrational peaks at >350 cm⁻¹ indicates that these Cu-induced modes introduce vibronic coupling, resulting in a broader distribution of the mid-gap electronic state at 300 K. Moreover, the IPR values in Figure 4d consistently show higher charge localization for the mid-gap state of surf-QD than the core-QD. The charge density of the defect state remains localized on the surface CuSe₃ cluster over the simulation time. As discussed, such charge localization makes the corresponding energy state subtle to the thermal fluctuations.

Thus, the vibrational characteristics and electronic nature of mid-gap states synergistically provide a largely oscillating defect state in the surf-QD. The core-QD, however, depicts that the substantially higher RMSF of the Cu does not eventually impact the energy state position much. The charge density plots at various instantaneous timeframes show that the Cu dopant and three Se atoms of the CuSe_4 cluster dominantly contribute to the defect state (Figure S15e). The most dynamic Cu-Se bond that forms and breaks periodically, as shown in Figure 3b, does not influence the charge density of the mid-gap state. Thus, even though the core Cu atom is dynamically active and possesses significant directional motion, the defect level remains much narrowly distributed for core-QD. Our simulations emphasize that atomistic details of local geometry and the nature of chemical bonding between dopant and host lattice dominate the vibronic coupling in these QDs.

The emission properties of Cu-doped CdSe QDs are extensively explored for optoelectronics.^{92,93} The localized hole in the defect state and delocalized electron in the conduction band radiatively recombine to produce broad emission in these doped QDs.⁹⁴ In this regard, one of the competing processes is non-radiative recombination which may dominate in the strong vibronic coupling regimes.^{95,96} To explore the probable impact of vibronic coupling, we calculate the phonon influence spectra for Cu-doped QDs. The Fourier transformation of the autocorrelation function of the energy gap between the conduction band edge and defect state is used for these influence spectra as shown in Figure 5b.⁹⁷ These spectra indicate the number and frequency of phonon modes involved with an electronic transition, resulting in non-radiative relaxation of carriers. The absence of peaks above 250 cm^{-1} in influence spectra matches well with the fact that there are no high-frequency vibrational modes in these QDs as already shown in the vDOS spectra in Figure S15a,b. In Figure 5b, the surf-QD exhibits a higher number of peaks, designating the coupling of more phonon modes with the CBM-defect state transition. The significant fluctuation of the mid-gap state position at 300 K eventually activates more phonon modes to undergo vibronic coupling for surf-QD. The spectra also reveal

multiple high-frequency peaks at and above 200 cm^{-1} that are largely absent in core-QD. These high-frequency phonon modes are contributed mainly by the surface Cu atom dynamics, as shown in Figure 3d. The number and high frequencies of active phonon modes designate that the surf-QD exhibits stronger vibronic coupling and may give rise to faster non-radiative recombination than that in the core-QD. The activation of non-radiative channels can substantially hamper the radiative emission processes in these CdSe QDs.

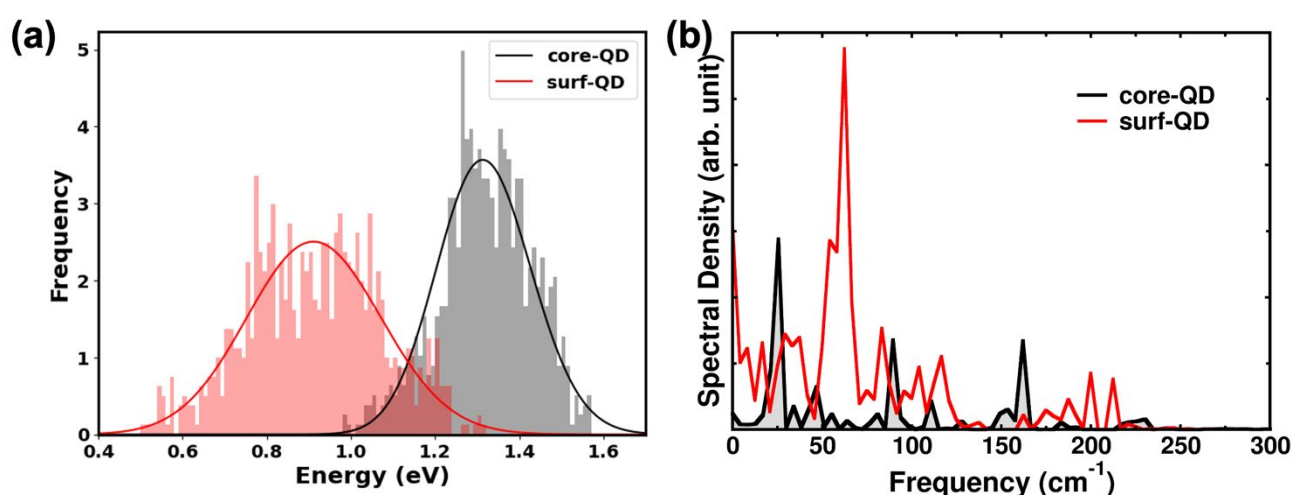


Figure 5. (a) Histogram of the gap value between the defect and CBM state over time and (b) corresponding influence spectra for core-QD and surf-QDs. The defect-CBM gap varies more widely, involving more high-frequency vibrational modes for surf-QD.

Overall, it is evident that the significant variations in the basic electronic structure and its coupling with vibrational subsystems arise due to differently positioned Cu dopants in the CdSe QDs. Consequently, we predict sizable dot-to-dot differences in optoelectronic properties, such as the emission energy distribution and radiative recombination rates in an ensemble of doped QDs. These are closely in line with several reported experimental observations.^{44,98,99} Our study emphasizes the importance of controlled synthetic protocols to selectively dope the small colloidal CdSe QD core with Cu atoms for consistent and narrow emission properties. The fine-tuning of the experimental conditions and appropriate choice of solvent medium for controlled cation exchange in colloidal synthesis is essential to achieve selective core doping of CdSe.

Finally, we explore different experimentally feasible approaches that can boost the emission properties of stable surf-QD. First, the photophysical properties of surf-QD are explored at low temperatures, 50 and 100 K. The plotted pair distribution functions $g(r)$ for Cd-Se and Cu-Se in Figure S19a demonstrate that the distribution of bond distances narrows down as the temperature decreases. Furthermore, the reduction in RMSD and RMSF values, as in Figure S19b,c confirm the suppressed structural fluctuations in surf-QD at low temperatures. Figure S18d demonstrates the histogram plot of mid-gap defect state positions at 50 K, 100 K, and 300 K for surf-QD. The distribution is much broader at 300 K, while it becomes narrower as the temperature decreases. The standard deviations for defect state position are 0.051, 0.087, and 0.139 for 50, 100, and 300K, respectively. These simulations show that reduced temperature leads to suppressed thermal fluctuation, narrowing the mid-gap defect state distribution over time. Thus, we expect a narrow emission linewidth from these surface-doped QDs at low temperatures. The experimental reports also indicate that one can enhance the color purity of emissive QDs by treating those at low temperatures, directly validating our computational findings.¹⁰⁰

Compositional engineering by including different-sized anions and cations at the neighboring coordination sites of Cu is another chemically viable approach to modify the optoelectronics of surf-QD. The local surface strain imposed by small-sized Cu can entirely or partially be relaxed by including large-sized cations or anions on the nearest site. In this regard, Ag and Te can be considered as these are already studied extensively for doping CdSe QDs.^{101,102} We will soon perform a detailed in-silico study on the effect of codoping of semiconductor QDs.

Conclusion:

To conclude, we employ first-principle simulations for exploring the impact of spatial heterogeneity of Cu doping in the optoelectronics of CdSe QDs. The Cu atom on the surface is more stable than core or subsurface sites, indicating the self-purification of these doped QDs

under suitable conditions. The dopant also includes a spin-polarized impurity state which can vary its mid-gap position depending on the location of Cu-site. The defect state remains close to the VBM edge for core-QD, whereas it moves to a deeper region for sub- and surface-QD. The antibonding overlap and extent of local Cu-Se bond contraction cause the variation in the energetics of the impurity state inside the band gap. Thorough analyses of structural dynamics at 300 K further reveal that the doped QDs remained structurally stable; however, dopant atoms exhibit larger fluctuations than host elements (Cd and Se), especially in the core-QD. Moreover, the vibrational features point out the presence of a few high-frequency modes contributed by the Cu on the surface. The electronic structures over time show a wide distribution of deep mid-gap levels for surf-QD, depicting its intricate response toward structural distortions at ambient conditions. The influence spectra further emphasize that more active vibrational modes couple to the conduction band to defect-state electronic transition in surf-QDs. These insights reveal the complex relationships among several intrinsic and extrinsic physicochemical characteristics, such as bonding type (bonding versus antibonding), local coordination geometry (surface versus core), and the extent of vibronic coupling (weak versus strong). All these factors dominantly influence the photophysical properties of Cu-doped CdSe QDs. We stress that successfully incorporating and stabilizing Cu on the CdSe QD core can substantially improve its color purity and exhibit narrow emission linewidth. Considering surf-QD, several experimentally viable approaches are suggested for strategically modifying their electronic structure and photophysics. Overall, our study provides invaluable atomistic insights into the dynamic structure-property relationship in Cu-doped CdSe, which can certainly guide the design of controlled experiments to realize improved optoelectronics in those nanomaterials.

Computational Methodology: We employ density functional theory (DFT) and *ab initio* molecular dynamics (AIMD) as implemented in the CP2K package to study the static and dynamic properties of QDs.^{103–105} For static simulations, we use spin-polarized DFT, whereas to explore the dynamic properties at ambient temperature, AIMD simulations are performed.¹⁰⁶

All these simulations utilize mixed Gaussian and plane-wave methods (GPW) with a cut-off of 350 Ry and the analytical dual-space pseudopotentials.^{107,108} A single Γ -point is used as the k -mesh due to the nonperiodic geometries of QDs where an average vacuum of 1.7 nm in all three directions is included.¹⁰⁹ The general gradient approximation (GGA) as prescribed by Perdew, Burke, and Ernzerhof is employed for approximating exchange and correlation interactions.^{107,108,110} Using the conjugate gradient method, the geometries of pristine and doped QDs are relaxed until the forces on each atom become less than 0.01 eV/Å.¹¹¹

An almost spherical pristine Cd₃₃Se₃₃ QD with a diameter of 1.28 nm is modeled by starting from bulk wurtzite CdSe.^{12,27,70,77} We examine doping energetics by calculating the formation enthalpy, $H_{\text{form.}} = [(E_{\text{undoped}}) - (E_{\text{doped}} + E_{\text{Cu}} - E_{\text{Cd}})]$, where E_{undoped} energy of pristine QD and E_{doped} , E_{Cu} and E_{Cd} are the energy of Cu doped QDs, the energy of single atom of Cu and Cd, respectively. The charge density difference and Bader charge analysis algorithm determine the net atomic charges and bonding nature of the defect state. The inverse participation ratio (IPR) for electronic states is calculated using the formalism used by Abteu et al. and some of us.^{55,70,112} Here, all the computational simulations of doped QDs are performed in their neutral charge state.

To study the structural dynamics of pristine and doped CdSe QDs at ambient conditions, we perform AIMD with the canonical ensemble (NVT). The Noose-Hover thermostat is used to maintain the temperature of the QD systems. A time step of 1 fs is used to integrate the equation of motion and generate trajectories of 16 ps, the last 10 ps of which are considered for all further analyses. The time-dependent electronic structures are calculated using self-consistent calculations on instantaneous geometries chosen after every 10 fs from the last 8 ps trajectories (total 800 snapshots). To study the influence of solvents, a few simulations include a polarizable continuum medium (PCM) employing a suitable dielectric constant, as considered previously.^{37,38,113} Some electronic structure calculations use Vienna Ab Initio Simulation

Package (VASP), as specifically mentioned. To study the influence of solvents, a few simulations include a polarizable continuum medium (PCM) employing a suitable dielectric constant, as considered previously.^{37,38,113} Some electronic structure calculations use the Vienna Ab Initio Simulation Package (VASP), as specifically mentioned.^{12,27,37,53,70} Further details on computational methods are included in Section S5 in Supporting Information (SI).

ASSOCIATED CONTENT

Supporting Information.

Details of optimized structures of pristine and doped-QDs, positional heterogeneity, oxidation state of Cu, ligand effect, solvent effects on pDOS, and band-edge and defect state charge densities. The electronic structure fluctuations at 50, 100, and 300 K.

AUTHOR INFORMATION

Corresponding Author

* Dibyajyoti Ghosh – Department of Materials Science and Engineering and Department of Chemistry, Indian Institute of Technology, Delhi, New Delhi 110016, India; orcid.org/0000-0002-3640-7537; Email: dibyajyoti@iitd.ac.in

Author contributions

PD and KS have performed all the simulations and analysed the data. DG has supervised the work, analysed the data. All authors have written the manuscript.

CONFLICT OF INTEREST

The authors declare no competing financial interest.

ACKNOWLEDGMENT

DG acknowledges the IIT Delhi SEED Grant (PLN12/04MS), the Science and Engineering Research Board (SERB), Department of Science and Technology (DST), India for Start-up Research Grant SRG/2022/001234 and the IIT Delhi HPC facility for computational resources. This work was performed, in part, at the Center for Integrated Nanotechnologies, an Office of Science User Facility operated for the U.S. Department of Energy (DOE) Office of Science by Los Alamos National Laboratory (Contract 89233218CNA000001) and Sandia National Laboratories (Contract DE-NA-0003525).

References:

- 1 S. Jana, B. B. Srivastava, S. Acharya, P. K. Santra, N. R. Jana, D. D. Sarma and N. Pradhan, *Chemical Communications*, 2010, **46**, 2853–2855.
- 2 C. Pu, X. Dai, Y. Shu, M. Zhu, Y. Deng, Y. Jin and X. Peng, *Nat Commun*, , DOI:10.1038/s41467-020-14756-5.
- 3 F. P. García de Arquer, D. V. Talapin, V. I. Klimov, Y. Arakawa, M. Bayer and E. H. Sargent, *Science*, 2021, 373.
- 4 V. I. Klimov, S. A. Ivanov, J. Nanda, M. Achermann, I. Bezel, J. A. McGuire and A. Piryatinski, *Nature*, 2007, **447**, 441–446.
- 5 M. C. Yen, C. J. Lee, K. H. Liu, Y. Peng, J. Leng, T. H. Chang, C. C. Chang, K. Tamada and Y. J. Lee, *Nat Commun*, , DOI:10.1038/s41467-021-24762-w.
- 6 I. J. Kramer and E. H. Sargent, *ACS Nano*, 2011, **5**, 8506–8514.
- 7 D. V. Talapin, J. S. Lee, M. V. Kovalenko and E. V. Shevchenko, *Chem Rev*, 2010, **110**, 389–458.
- 8 O. Volnianska, M. Szymura, J. Mikulski and Kłopotowski, *Journal of Physical Chemistry C*, 2021, **125**, 16827–16836.
- 9 L. S. Li, J. Hu, W. Yang and A. P. Alivisatos, *Nano Lett*, 2001, **1**, 349–351.
- 10 M. C. Tropicovsky, L. Kronik and J. R. Chelikowsky, *Journal of Chemical Physics*, 2003, **119**, 2284–2287.

- 11 B. Alpers, I. Rubinstein and G. Hodes, *Phys Rev B Condens Matter Mater Phys*, , DOI:10.1103/PhysRevB.63.081303.
- 12 A. Kasuya, R. Sivamohan, Y. A. Barnakov, I. M. Dmitruk, T. Nirasawa, V. R. Romanyuk, V. Kumar, S. V. Mamykin, K. Tohji, B. Jeyadevan, K. Shinoda, T. Kudo, O. Terasaki, Z. Liu, R. V. Belosludov, V. Sundararajan and Y. Kawazoe, *Nat Mater*, 2004, **3**, 99–102.
- 13 T. Galle, M. Kazes, R. Hübner, J. Lox, M. Samadi Khoshkhoo, L. Sonntag, R. Tietze, V. Sayevich, D. Oron, A. Koitzsch, V. Lesnyak and A. Eychmüller, *Chemistry of Materials*, 2019, **31**, 5065–5074.
- 14 D. Bera, L. Qian, T. K. Tseng and P. H. Holloway, *Materials*, 2010, **3**, 2260–2345.
- 15 L. Zhang, H. Yang, Y. Tang, W. Xiang, C. Wang, T. Xu, X. Wang, M. Xiao and J. Zhang, *Chemical Engineering Journal*, , DOI:10.1016/j.cej.2021.131159.
- 16 M. Bhati, S. A. Ivanov, T. P. Senftle, S. Tretiak and D. Ghosh, *Nanoscale*, , DOI:10.1039/d2nr06785d.
- 17 M. J. Almendral-Parra, A. Alonso-Mateos, J. F. Boyero-Benito, S. Sánchez-Paradinas and E. Rodríguez-Fernández, *J Nanomater*, , DOI:10.1155/2014/397469.
- 18 M. Bhati, S. A. Ivanov, T. P. Senftle, S. Tretiak and D. Ghosh, *J Mater Chem A Mater*, 2021, **10**, 5212–5220.
- 19 M. A. Boles, D. Ling, T. Hyeon and D. V. Talapin, *Nat Mater*, 2016, **15**, 141–153.
- 20 C. L. Hartley, M. L. Kessler and J. L. Dempsey, *J Am Chem Soc*, 2021, **143**, 1251–1266.
- 21 S. A. Fischer, A. M. Crotty, S. V. Kilina, S. A. Ivanov and S. Tretiak, *Nanoscale*, 2012, **4**, 904–914.
- 22 P. Wu and X. P. Yan, *Chem Soc Rev*, 2013, **42**, 5489–5521.
- 23 H. J. Queisser and E. E. Haller, *Defects in Semiconductors: Some Fatal, Some Vital*, .
- 24 R. Rabeya, S. Mahalingam, A. Manap, M. Satgunam, M. Akhtaruzzaman and C. H. Chia, *Int J Quantum Chem*, 2022, 122.
- 25 F. Zhao, S. Hu, C. Xu, H. Xiao, X. Zhou, X. Zu and S. Peng, *Nanomaterials*, , DOI:10.3390/nano11102531.
- 26 H. X. Deng, J. W. Luo, S. S. Li and S. H. Wei, *Phys Rev Lett*, , DOI:10.1103/PhysRevLett.117.165901.
- 27 R. Viswanatha, S. Brovelli, A. Pandey, S. A. Crooker and V. I. Klimov, *Nano Lett*, 2011, **11**, 4753–4758.
- 28 F. A. Zhao, H. Y. Xiao, X. M. Bai and X. T. Zu, *Physical Chemistry Chemical Physics*, 2019, **21**, 16108–16119.
- 29 K. E. Knowles, K. H. Hartstein, T. B. Kilburn, A. Marchioro, H. D. Nelson, P. J. Whitham and D. R. Gamelin, *Chem Rev*, 2016, **116**, 10820–10851.
- 30 N. Pradhan, S. Das Adhikari, A. Nag and D. D. Sarma, *Angewandte Chemie*, 2017, **129**, 7144–7160.
- 31 A. Harchol, Y. Barak, K. E. Hughes, K. H. Hartstein, H. J. Jöbsis, P. T. Prins, C. De Mello Donegá, D. R. Gamelin and E. Lifshitz, *ACS Nano*, 2022, **16**, 12866–12877.
- 32 A. N. Yazici, M. Öztaş and M. Bedir, *Opt Mater (Amst)*, 2007, **29**, 1091–1096.
- 33 K. E. Hughes, S. R. Ostheller, H. D. Nelson and D. R. Gamelin, *Nano Lett*, 2019, **19**, 1318–1325.
- 34 A. M. Smirnov, A. D. Golinskaya, P. A. Kotin, S. G. Dorofeev, V. V. Palyulin, V. N. Mantsevich and V. S. Dneprovskii, *J Lumin*, 2019, **213**, 29–35.
- 35 A. J. Houtepen, Z. Hens, J. S. Owen and I. Infante, *Chemistry of Materials*, 2017, **29**, 752–761.
- 36 S. Kilina, K. A. Velizhanin, S. Ivanov, O. V. Prezhdo and S. Tretiak, *ACS Nano*, 2012, **6**, 6515–6524.

- 37 H. D. Nelson, X. Li and D. R. Gamelin, *Journal of Physical Chemistry C*, 2016, **120**, 5714–5723.
- 38 P. Senellart, G. Solomon and A. White, *Nat Nanotechnol*, 2017, **12**, 1026–1039.
- 39 R. S. Daveau, K. C. Balram, T. Pregnoiato, J. Liu, E. H. Lee, J. D. Song, V. Verma, R. Mirin, S. W. Nam, L. Midolo, S. Stobbe, K. Srinivasan and P. Lodahl, *Optica*, 2017, **4**, 178.
- 40 T. P. Nguyen, T. T. Ha, T. T. Nguyen, N. P. Ho, T. D. Huynh and Q. V. Lam, *Electrochim Acta*, 2018, **282**, 16–23.
- 41 M. G. Taylor and H. J. Kulik, *Chemistry of Materials*, 2021, **33**, 7113–7123.
- 42 S. Brovelli, C. Galland, R. Viswanatha and V. I. Klimov, *Nano Lett*, 2012, **12**, 4372–4379.
- 43 S. C. Erwin, L. Zu, M. I. Haftel, A. L. Efros, T. A. Kennedy and D. J. Norris, *Nature*, 2005, **436**, 91–94.
- 44 J. Zhang, Q. Di, J. Liu, B. Bai, J. Liu, M. Xu and J. Liu, *Journal of Physical Chemistry Letters*, 2017, **8**, 4943–4953.
- 45 A. S. Fuhr, P. Sautet and A. N. Alexandrova, *Journal of Physical Chemistry C*, 2019, **123**, 5705–5713.
- 46 A. Khammang, J. T. Wright and R. W. Meulenber, *Nat Commun*, , DOI:10.1038/s41467-020-20712-0.
- 47 A. N. Beecher, R. A. Dziatko, M. L. Steigerwald, J. S. Owen and A. C. Crowther, *J Am Chem Soc*, 2016, **138**, 16754–16763.
- 48 H. D. Nelson, S. O. M. Hinterding, R. Fainblat, S. E. Creutz, X. Li and D. R. Gamelin, *J Am Chem Soc*, 2017, **139**, 6411–6421.
- 49 M. G. Taylor and H. J. Kulik, *Chemistry of Materials*, 2021, **33**, 7113–7123.
- 50 V. Sayevich, Z. L. Robinson, Y. Kim, O. V. Kozlov, H. Jung, T. Nakotte, Y. S. Park and V. I. Klimov, *Nat Nanotechnol*, 2021, **16**, 673–679.
- 51 M. Makkar and R. Viswanatha, *RSC Adv*, 2018, **8**, 22103–22112.
- 52 S. Gul, J. K. Cooper, P. A. Glans, J. Guo, V. K. Yachandra, J. Yano and J. Z. Zhang, *ACS Nano*, 2013, **7**, 8680–8692.
- 53 S. Gumber, O. Eniodunmo, S. A. Ivanov, S. Kilina, O. V. Prezhdo, D. Ghosh and S. Tretiak, *J Mater Chem A Mater*, , DOI:10.1039/d3ta00149k.
- 54 S. Kudara, M. Zanella, C. Giannini, A. Rizzo, Y. Li, G. Gigli, R. Cingolani, G. Ciccarella, W. Spahl, W. J. Parak and L. Manna, *Advanced Materials*, 2007, **19**, 548–552.
- 55 S. M. Harrell, J. R. McBride and S. J. Rosenthal, *Chemistry of Materials*, 2013, **25**, 1199–1210.
- 56 A. M. Jawaid, S. Chattopadhyay, D. J. Wink, L. E. Page and P. T. Snee, *ACS Nano*, 2013, **7**, 3190–3197.
- 57 S. Kilina, S. Ivanov and S. Tretiak, *J Am Chem Soc*, 2009, **131**, 7717–7726.
- 58 L. Yang, K. E. Knowles, A. Gopalan, K. E. Hughes, M. C. James and D. R. Gamelin, *Chemistry of Materials*, 2016, **28**, 7375–7384.
- 59 F. Zhang, W. Zhang, D. Wexler and Z. Guo, *Advanced Materials*, 2022, **34**.
- 60 S. C. Erwin, L. Zu, M. I. Haftel, A. L. Efros, T. A. Kennedy and D. J. Norris, *Nature*, 2005, **436**, 91–94.
- 61 G. M. Dalpian and J. R. Chelikowsky, *Phys Rev Lett*, , DOI:10.1103/PhysRevLett.96.226802.
- 62 J. Owen and L. Brus, *J Am Chem Soc*, 2017, **139**, 10939–10943.
- 63 B. Car, S. Medling, C. Corrado, F. Bridges and J. Z. Zhang, *Nanoscale*, 2011, **3**, 4182–4189.
- 64 A. I. Goldman, E. Canova, Y. H. Kao, B. J. Fitzpatrick, R. N. Bhargava and J. C. Phillips, *Appl Phys Lett*, 1983, **43**, 836–838.

- 65 M. Dupraz, N. Li, J. Carnis, L. Wu, S. Labat, C. Chatelier, R. van de Poll, J. P. Hofmann, E. Almog, S. J. Leake, Y. Watier, S. Lazarev, F. Westermeier, M. Sprung, E. J. M. Hensen, O. Thomas, E. Rabkin and M. I. Richard, *Nat Commun*, , DOI:10.1038/s41467-022-30592-1.
- 66 S. Zhang, X. Zhang, G. Jiang, H. Zhu, S. Guo, D. Su, G. Lu and S. Sun, *J Am Chem Soc*, 2014, **136**, 7734–7739.
- 67 V. V. Albert, S. A. Ivanov, S. Tretiak and S. V. Kilina, *Journal of Physical Chemistry C*, 2011, **115**, 15793–15800.
- 68 A. Harchol, Y. Barak, K. E. Hughes, K. H. Hartstein, H. J. Jöbsis, P. T. Prins, C. De Mello Donegá, D. R. Gamelin and E. Lifshitz, *ACS Nano*, 2022, **16**, 12866–12877.
- 69 A. Pandey, S. Brovelli, R. Viswanatha, L. Li, J. M. Pietryga, V. I. Klimov and S. A. Crooker, , DOI:10.1038/NNANO.2012.210.
- 70 H. Zang, H. Li, N. S. Makarov, K. A. Velizhanin, K. Wu, Y. S. Park and V. I. Klimov, *Nano Lett*, 2017, **17**, 1787–1795.
- 71 A. S. Fuhr, H. J. Yun, N. S. Makarov, H. Li, H. McDaniel and V. I. Klimov, *ACS Photonics*, 2017, **4**, 2425–2435.
- 72 K. Kara-Zaitri, L. Bendaoudi, M. Ould-Mohamed and T. Ouahrani, *Mater Sci Semicond Process*, , DOI:10.1016/j.mssp.2022.106938.
- 73 A. E. Kuznetsov and D. N. Beratan, *Journal of Physical Chemistry C*, 2014, **118**, 7094–7109.
- 74 D. A. Fenoll, M. Sodupe and X. Solans-Monfort, *ACS Omega*, , DOI:10.1021/acsomega.3c00324.
- 75 A. J. Houtepen, Z. Hens, J. S. Owen and I. Infante, *Chemistry of Materials*, 2017, **29**, 752–761.
- 76 I. Du Fossé, S. C. Boehme, I. Infante and A. J. Houtepen, *Chemistry of Materials*, 2021, **33**, 3349–3358.
- 77 D. Ghosh, S. A. Ivanov and S. Tretiak, *Chemistry of Materials*, 2021, **33**, 7848–7857.
- 78 D. Ghosh, S. A. Ivanov and S. Tretiak, *Chemistry of Materials*, 2021, **33**, 7848–7857.
- 79 G. Henkelman, B. P. Uberuaga and H. Jónsson, *J Chem Phys*, 2000, **113**, 9901–9904.
- 80 M. Brehm, M. Thomas, S. Gehrke and B. Kirchner, *Journal of Chemical Physics*, 2020, 152.
- 81 A. N. Beecher, R. A. Dziatko, M. L. Steigerwald, J. S. Owen and A. C. Crowther, *J Am Chem Soc*, 2016, **138**, 16754–16763.
- 82 A. N. Beecher, R. A. Dziatko, M. L. Steigerwald, J. S. Owen and A. C. Crowther, *J Am Chem Soc*, 2016, **138**, 16754–16763.
- 83 I. Dmitruk, R. V. Belosludov, A. Dmytruk, Y. Noda, Y. Barnakov, Y. S. Park and A. Kasuya, *Journal of Physical Chemistry A*, 2020, **124**, 3398–3406.
- 84 C. Shi, A. N. Beecher, Y. Li, J. S. Owen, B. M. Leu, A. H. Said, M. Y. Hu and S. J. L. Billinge, *Phys Rev Lett*, , DOI:10.1103/PhysRevLett.122.026101.
- 85 A. I. Lebedev, B. M. Saidzhonov, K. A. Drozdov, A. A. Khomich and R. B. Vasiliev, *Journal of Physical Chemistry C*, 2021, **125**, 6758–6766.
- 86 C. Lin, D. F. Kelley, M. Rico and A. M. Kelley, *ACS Nano*, 2014, **8**, 3928–3938.
- 87 A. N. Beecher, R. A. Dziatko, M. L. Steigerwald, J. S. Owen and A. C. Crowther, *J Am Chem Soc*, 2016, **138**, 16754–16763.
- 88 I. Du Fossé, S. C. Boehme, I. Infante and A. J. Houtepen, *Chemistry of Materials*, 2021, **33**, 3349–3358.
- 89 A. Dutta, R. Bera, A. Ghosh and A. Patra, *Journal of Physical Chemistry C*, 2018, **122**, 16992–17000.
- 90 A. M. Smirnov, A. D. Golinskaya, P. A. Kotin, S. G. Dorofeev, V. V. Palyulin, V. N. Mantsevich and V. S. Dneprovskii, *J Lumin*, 2019, **213**, 29–35.
- 91 S. V. Kilina, P. K. Tamukong and D. S. Kilin, *Acc Chem Res*, 2016, **49**, 2127–2135.

- 92 A. M. Kelley, *Journal of Physical Chemistry Letters*, 2010, **1**, 1296–1300.
- 93 C. Lin, K. Gong, D. F. Kelley and A. M. Kelley, *ACS Nano*, 2015, **9**, 8131–8141.
- 94 A. V. Akimov and O. V. Prezhdo, *J Chem Theory Comput*, 2013, **9**, 4959–4972.
- 95 H. Zang, H. Li, N. S. Makarov, K. A. Velizhanin, K. Wu, Y. S. Park and V. I. Klimov, *Nano Lett*, 2017, **17**, 1787–1795.
- 96 D. A. Bussian, S. A. Crooker, M. Yin, M. Brynda, A. L. Efros and V. I. Klimov, *Nat Mater*, 2009, **8**, 35–40.
- 97 J. T. Siy, E. M. Brauser and M. H. Bartl, *Chemical Communications*, 2011, **47**, 364–366.
- 98 D. Morgan and D. F. Kelley, *Journal of Physical Chemistry C*, 2018, **122**, 10627–10636.
- 99 F. A. Zhao, H. Y. Xiao, X. M. Bai and X. T. Zu, *Physical Chemistry Chemical Physics*, 2019, **21**, 16108–16119.
- 100 G. Kresse and J. Hafner, *Ab initio molecular dynamics for liquid metals*, vol. 47.
- 101 A. Jain, Y. Shin and K. A. Persson, *Nat Rev Mater*, 2016, 1.
- 102 T. D. Kühne, M. Iannuzzi, M. Del Ben, V. V. Rybkin, P. Seewald, F. Stein, T. Laino, R. Z. Khaliullin, O. Schütt, F. Schiffmann, D. Golze, J. Wilhelm, S. Chulkov, M. H. Bani-Hashemian, V. Weber, U. Borštnik, M. Taillefumier, A. S. Jakobovits, A. Lazzaro, H. Pabst, T. Müller, R. Schade, M. Guidon, S. Andermatt, N. Holmberg, G. K. Schenter, A. Hehn, A. Bussy, F. Belleflamme, G. Tabacchi, A. Glöß, M. Lass, I. Bethune, C. J. Mundy, C. Plessl, M. Watkins, J. VandeVondele, M. Krack and J. Hutter, *Journal of Chemical Physics*, 2020, 152.
- 103 K. K. Rao, Y. Yao, L. Christian and M. E. Tuckerman, *Ab initio molecular dynamics: basic concepts, current trends and novel applications You may also like Modeling of Transport Mechanisms of OH-in Electrolyte of Alkaline Fuel Cell Hiromitsu Takaba, Nobuyuki Shimizu, Tomoya Hisabe et al.-Accelerated Modeling of Lithium Diffusion in Solid State Electrolytes Using Artificial Neural Networks Ab initio molecular dynamics: basic concepts, current trends and novel applications*, 2002, vol. 14.
- 104 J. VandeVondele and J. Hutter, *Journal of Chemical Physics*, 2003, **118**, 4365–4369.
- 105 J. P. Perdew, A. Ruzsinszky, G. I. Csonka, O. A. Vydrov, G. E. Scuseria, L. A. Constantin, X. Zhou and K. Burke, *Phys Rev Lett*, , DOI:10.1103/PhysRevLett.100.136406.
- 106 H. S. Patel, V. A. Dabhi and A. M. Vora, *Mater Today Proc*, 2022, **57**, 275–278.
- 107 J. P. Perdew, K. Burke and M. Ernzerhof, *Generalized Gradient Approximation Made Simple*, 1996.
- 108 J. R. Shewchuk, *An Introduction to the Conjugate Gradient Method Without the Agonizing Pain*, 1994.
- 109 T. A. Abtew and D. A. Drabold, *Phys Rev B Condens Matter Mater Phys*, , DOI:10.1103/PhysRevB.74.085201.
- 110 S. Ten Brinck, F. Zaccaria and I. Infante, *ACS Energy Lett*, 2019, **4**, 2739–2747.